Progress In Electromagnetics Research B, Vol. 84, 79–96, 2019

Radiation Pattern Analysis and Modelling of Coplanar Vivaldi Antenna Element for Linear Array Pattern Evaluation

Nurhayati[1, 2, *], Eko Setijadi[1], and Gamantyo Hendrantoro[1]

Abstract—This paper reports an electric field approximation model of the Coplanar Vivaldi antenna on the E-plane. The study is conducted in three stages, i.e., (i) evaluating the impact of various geometrical parameters to the Vivaldi's element performance at different frequencies, (ii) modeling the electric field patterns, and (iii) applying the model to evaluate the linear total array pattern. The examination of the Coplanar Vivaldi element with fractional bandwidth of 133% in the 2–10 GHz band shows the individual roles of the antenna width, the tapered slot length, the opening width and the slope of the tapered slot in determining the VSWR, resistance, reactance and E-Field performance. The Vivaldi element should be designed with element width more than 0.5λ and less than λ to reach better performance of VSWR and E-field. The longer the tapered slot ($> \lambda$) with the high value of opening rate of tapered slot, the smaller the E-field. The E-field increases with increasing opening width of the tapered slot. Knowledge of the influence of each geometry parameter is then used as a reference in developing the E-field pattern approximation model of the Vivaldi element. The derivation of the Vivaldi approximation model is started from the pattern of a horn antenna because both antennas share a similar feature, i.e., the enclosure of the E-field propagation within a tapered slot resulting in a directional radiation pattern. The result of Coplanar Vivaldi modeling is verified against the results of electromagnetic computational simulation and measurement. The Vivaldi element model is useful for total array pattern analysis to save computation time and to provide flexibility in the evaluation of array design.

1. INTRODUCTION

Vivaldi antenna is a planar antenna with a light weight, low profile, wide bandwidth, directional radiation pattern, and high gain [1–4] Vivaldi antenna can be applied for through-wall detection [5], imaging [6], radar [7, 8] and communication [9]. Many studies on Vivaldi antenna have been aimed to improve the performance, using numerical electromagnetic computation for evaluation. Bandwidth and radiation pattern performance of Vivaldi antenna depends on the geometry such as the length and the width, the mouth opening of tapered slot and the slope of tapered slot. The feeding shape, the radiator shape and the substrate also predispose the bandwidth and radiation pattern performance.

In terms of the design structure, Vivaldi antennas can be divided into three classes, i.e., Coplanar Vivaldi Antenna, Antipodal Vivaldi Antenna (AVA) and Balanced Antipodal Vivaldi Antenna (BAVA), each with its own strengths. For instance, the family of AVA generally shows high gain and wide [10–12]. However, the wide bandwidth implies the emergence of grating lobes when the antennas are used in array configuration especially in high frequency region of the band [13]. Accordingly, in this paper, we focus on Coplanar Vivaldi antenna.

Parametric studies of several dimensions of Vivaldi antenna with respect to impedance and VSWR performance have been published in [14, 15]. However, while in a Vivaldi array the element pattern

Received 5 April 2019, Accepted 22 May 2019, Scheduled 14 June 2019

* Corresponding author: Nurhayati (nurhayati15@mhs.ee.its.ac.id).

[1] Department of Electrical Engineering, Institut Teknologi Sepuluh Nopember, Surabaya 60111, Indonesia. [2] Departement of Electrical Engineering, Universitas Negeri Surabaya, Indoesia, Surabaya 60231, Indonesia.

contributes the total array pattern [16, 17], parametric study of the Coplanar Vivaldi geometry with respect to the radiation pattern is still limited. Our first goal is to analyze the effect of geometry variation on VSWR, impedance and radiation pattern performance, that can be reference to design antenna element which will be discussed in Section 2.

Antenna array can enlarge gain, reduce beam width, and cover certain beam scanning [18]. On the other hand, arrays with uniform spacing suffer from mutual coupling [19], which for those with Coplanar Vivaldi elements can be mitigated by employing corrugated and/or truncated slot structures [13]. An example of large Vivaldi arrays are those with hundreds of elements that have been used in astronomy and telescope application. Array optimization, especially for those with a very large number of elements [20, 21], e.g., up to hundreds or thousands of them, requires very long computation time. It also requires a high-grade computer to analyze large Vivaldi array with electromagnetic numerical computation. In actual analysis, array optimization can be done by analytical methods so that the computation process can be made more flexible with signal processing techniques and, hence, faster. However, use of analytical method requires antenna element modelling.

Most analytical methods for array antenna have been reported by focusing on commonly used elements, such as isotropic [22], dipole [23], and microstrip [24]. Discussions of radiation pattern analysis of linear tapered slot antenna and slot line have been reported in [25, 26]. Nevertheless, the computational radiation pattern which is employed using the moment method by developing basis functions results in a more complex algorithm. For an antenna array, the total pattern can be obtained analytically by multiplying the E-field pattern of the element with the array factor. However, the mathematical expression for radiation pattern of a Vivaldi element is presently not available for use in Vivaldi array pattern analysis. Thus far, pattern analysis of a Vivaldi array must resort to computational electromagnetic algorithms. Therefore, it is necessary to develop analysis and modelling of the radiation pattern of a Vivaldi antenna which is related to its geometry and working frequency.

Horn and Vivaldi antennas have similarities in the presence of tapered structure and directional radiation pattern [27]. While horn is a volume antenna, Vivaldi antenna is planar. Both antennas have electric fields that propagate between the sides of the tapered structure.

The second objective of this paper is to develop a novel radiation pattern model of Vivaldi element using the same approach as used for horn antenna, to be discussed in Section 3. The use of such a mathematical model can reduce computation time and make analytical calculations more flexible. We evaluate the accuracy of the Coplanar Vivaldi element pattern model in Section 4 and the total array pattern obtained by pattern multiplication in Section 5 through comparison with results from CST simulation. Finally, Section 5 concludes this paper.

2. PARAMETER STUDY OF GEOMETRY

We start with the design of Vivaldi antenna element as shown in Fig. 1, in which FR4 substrate is used with permittivity of 4.6, substrate thickness of 1.6 mm, and copper thickness of 0.035 mm. It is designed

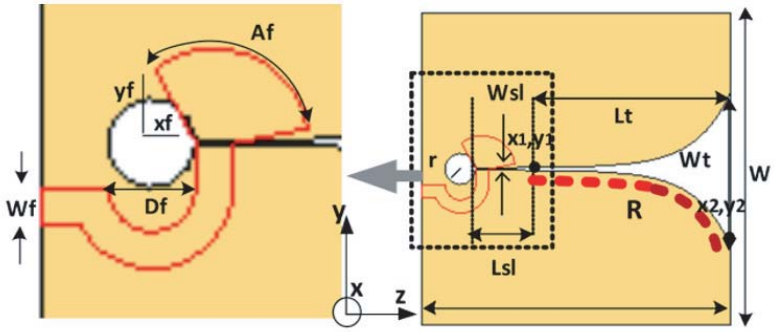

Figure 1. Dimension of a Vivaldi antenna [16], with R is opening slope/opening rate of tapered slot.

with slope of tapered slot as follows [13]:

$$y = C_1 e^{Rx} + C_2, \quad C_1 = \frac{y_2 - y_1}{e^{Rx_2} - e^{Rx_1}}, \quad C_2 = \frac{y_1 e^{Rx_2} - y_2 e^{Rx_1}}{e^{Rx_2} - e^{Rx_1}} \tag{1}$$

where x and y denote coordinates in cartesian system; R is the slope of the tapered; (x_1, y_1) and (x_2, y_2) are the coordinates of the start and end of the tapered slot, respectively.

The Vivaldi antenna is designed to achieve a bandwidth of 133% based on VSWR (Voltage Standing Wave Ratio) of less than 2 in the 2–10 GHz range. The next step is to vary one of the antenna's geometries and make the others fixed, without changing the shape of feed line and the type of substrate. The detailed design parameters of Coplanar Vivaldi Element as shown in Fig. 1 are listed in Table 1.

Table 1. Geometry of antenna element based on Figure 1.

Parameter	Dimension (mm)	Parameter	Dimension (mm)
L	60	r	3
W	60	W_f	2.5
W_t	30	D_f	3
L_t	42.5	x_f	4
L_{sl}	7.5	y_f	5
W_{sl}	0.5	R	0.15

2.1. Antenna Width

Figure 2(a) shows the variation in VSWR due to variation of antenna width (W) by setting $L = 60$ mm, $W_t = 30$ mm, $R = 0.15$. Figure 2(a) shows VSWR for $W = 40$ mm, which at 2 GHz corresponds to 0.267λ and results in VSWR > 2. It happens because the antenna is designed with $W < 0.5\lambda$ and indicates the occurrence of impedance mismatch between the radiator and free space so that the

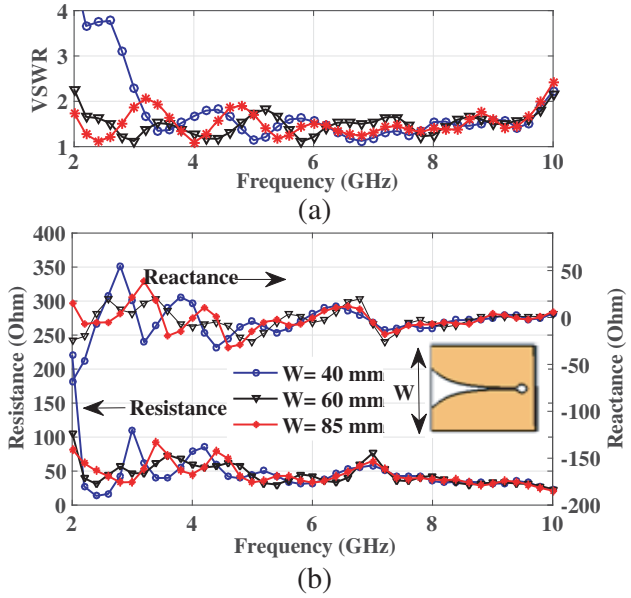

Figure 2. Effect of element width to (a) VSWR, and (b) resistance and reactance performance with $L = 60$ mm, $W_t = 30$ mm, $R = 0.15$.

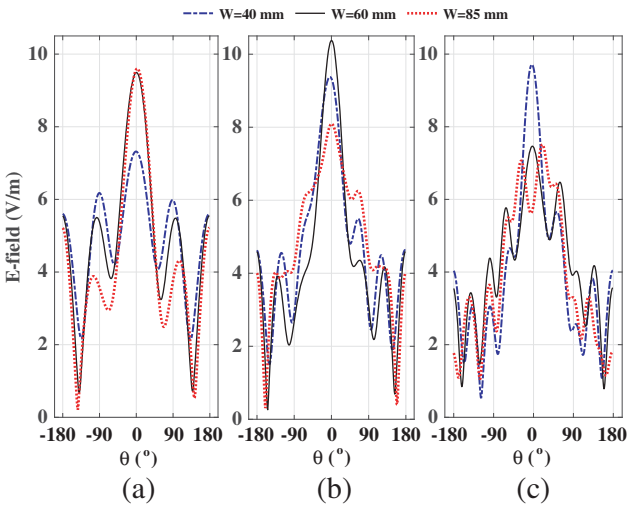

Figure 3. E-field on the E-plane with various element width at (a) 3 GHz, (b) 5 GHz and (c) 7 GHz with $L = 60$ mm, $W_t = 30$ mm, $R = 0.15$.

maximum power transfer is not fulfilled. At 3 GHz, the element width of 40 mm corresponds to 0.4λ, 60 mm to 0.6λ and 80 mm to 0.8λ. The result shows that an element width of more than 0.5λ with respect to its operating frequency results in VSWR < 2 and, therefore, can be considered in antenna design as a reference to achieve the desired VSWR performance at the lowest frequency. Figure 2(b) presents the performance of resistance (bottom curve) and reactance (upper curve) for varying element width. Vivaldi antennas with an element width less than half wavelength demonstrate high resistance at the low-end frequency as shown in the lower curve of Figure 2(b). It also shows the fluctuation of reactance as shown in the upper side of Figure 2(b).

Figure 3 shows the E-field patterns obtained by changing the element width at frequencies of 3, 5, and 7 GHz. At 3 GHz (see Figure 3(a)), the Vivaldi antenna with element width of 40 mm or 0.4λ has the smallest E-field and VSWR > 2. The size also produces high resistance and reactance and influences radiation pattern. Also at 3 GHz, the wider antennas yield higher E-fields for element width not more than 1λ. The figure also exhibits that the SLL performance ranges from best to worst for $W = 80$ mm, 60 mm and 40 mm, respectively. The E-field performance at 5 GHz (see Figure 3(b)) is reached from best to worst for $W = 60$ mm (1λ), $W = 40$ mm (0.667λ) and $W = 80$ mm (1.33λ), respectively. Meanwhile at 7 GHz, the E-field performance is obtained for $W = 40$ mm (0.93λ), $W = 60$ mm (1.4λa) and $W = 80$ mm (1.86λ), successively, from best to worst. An antenna with the element width of more than 0.5λ but less than 1λ has better E-field than others. Although an antenna has VSWR < 2, the E-field at the high-end frequency depends on the width of antenna relative to its wavelength.

If the antenna element width is more than 1λ, it will yield a worse E-field than those with width less than 1λ. It can be seen in Figure 5 that at frequency 7 GHz, antenna width of 85 mm (1.85λ) yields more side lobes. Higher frequencies causes higher side lobe levels (SLL). From the description above it can be concluded that the antenna with element width less than 0.5λ will yield VSWR more than two, suffer from fluctuation of resistance and reactance, show a decrease in E-field and increase in the SLL (at low-end frequencies). Moreover, if an antenna is designed with element width more than 1λ, although it has VSWR less than 2, it degrades the E-field performance especially at the high-end frequency band, which causes high side lobe. Thus, it is necessary to design antenna by considering the element width relative to its desired operating frequency.

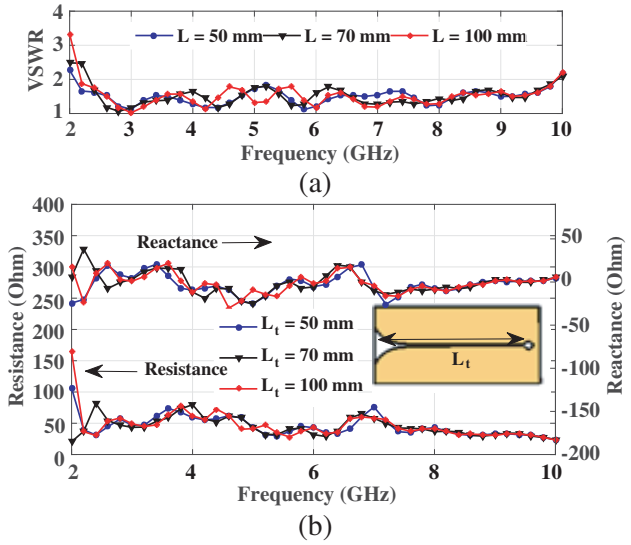

Figure 4. Effect of of element length to (a) VSWR, resistance and reactance performance $W = 60$ mm, $W_t = 30$ mm, $R = 0.15$.

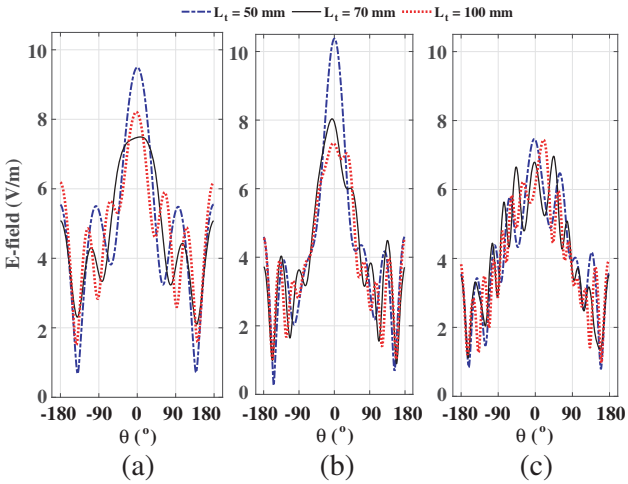

Figure 5. E-field on the E-plane with various element length at (a) 3 GHz, (b) 5 GHz and (c) 7 GHz $W = 60$ mm, $W_t = 30$ mm, $R = 0.15$.

2.2. Length of the Tapered Slot

VSWRs and impedance performances with various lengths of tapered slot (L_t) are shown in Figure 4, taken for $W = 60\,\text{mm}$, $W_t = 30\,\text{mm}$, $R = 0.15$. The VSWR at the low-end frequency (2 GHz) descends with the decreasing length, i.e., at $L_t = 100\,\text{mm}$ (0.67λ), $L_t = 70\,\text{mm}$ (0.47λ) and $L_t = 50\,\text{mm}$ (0.33λ) consecutively, reveals that longer size of tapered slot yields higher resistance, but the reactance alternates insignificantly. If the length of tapered slot is extended, but the opening rate is fixed, and the tapered slot opening mouth is small, it will increase VSWR. References [14, 15] explain that with smaller flare angle, which is related to the slope of the tapered slot, longer tapered slot yields higher resistance and reactance at the low-end frequency. However, we simulate elements with the same value of $R = 0.15$ so that when the tapered slot is longer, VSWR becomes worse.

The effect of the length of tapered slot on the E field performance is depicted in Figure 5. At 3 GHz, a Vivaldi antenna with $L_t = 50\,\text{mm}$ (0.5λ) has higher E-field than that for $L_t = 100\,\text{mm}$ (1λ) and 70 mm (0.7λ). It also shows that increasing E-field appears for the length of tapered slot (L_t) in factor 0.5λ. It can be seen that tapered slot that has $L_t = 0.5\lambda$ and 1λ has better E-field compared to $L_t = 0.7\lambda$.

However, escalation of L_t with $R = 0.15$ while W remains small will yield worse E-field. At 5 GHz, by setting $L_t = 50\,\text{mm} \approx 0.83\lambda$, it yields an E-field higher than it does with $L_t = 70\,\text{mm} \approx 1.16\lambda$ and $L_t = 100\,\text{mm} \approx 1.667\lambda$. It shows that a longer tapered slot yields a smaller E-field. At 7 GHz, antennas with $L_t = 100\,\text{mm}$ (2.33λ), $L_t = 50\,\text{mm}$ (1.17λ) and $L_t = 70\,\text{mm}$ (1.63λ) produce poor radiation pattern. The longer the tapered slot ($> 1\lambda$) with the high value of R but small value of W yields a smaller E-field. A high value of R with a long tapered slot has a gradual slope in the beginning and the middle of the slot but with a drastic change at the end of tapered slot opening. This influences resonance at high frequency and yields high SLL, which is shown in Figure 5(c) and can be explained as follows. An antenna with a higher operating frequency has shorter wavelength than those at lower frequencies. For the same length of tapered slot (L_t) at high frequency, the antenna has more longer tapered slot relative to its wavelength than at lower frequency.

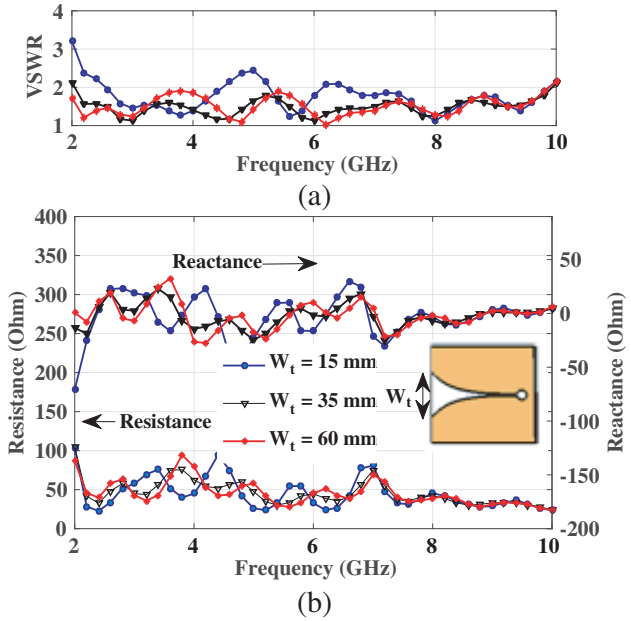

Figure 6. Effect of opening mouth of tapered tapered slot to (a) VSWR and (b) resistance and reactance $L_t = 50\,\text{mm}$, $W = 60\,\text{mm}$ and $R = 0.15$.

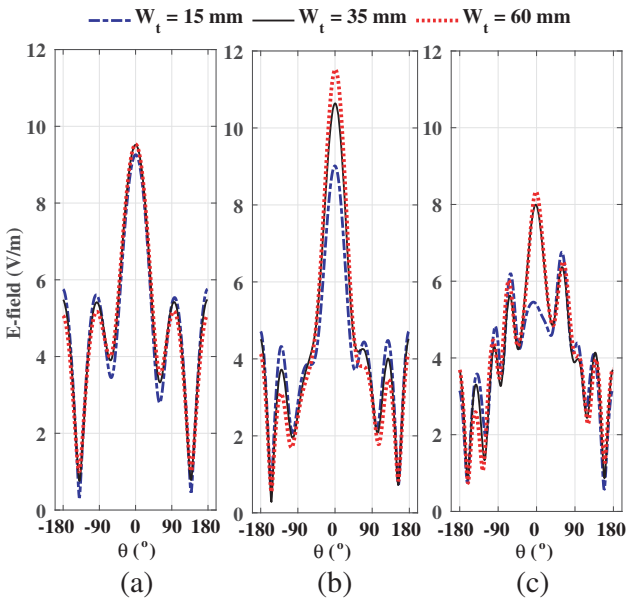

Figure 7. E-field on the E-plane with various opening mouth of tapered slot at frequency (a) 3 GHz, (b) 5 GHz and (c) 7 GHz $L_t = 50\,\text{mm}$, $W = 60\,\text{mm}$ and $R = 0.15$.

2.3. Opening Width of the Tapered Slot

The effects of the tapered slot opening size (W_t) on VSWR, resistance, and reactance performance are presented in Figure 6 with $L_t = 50\,\text{mm}$, $W = 60\,\text{mm}$ and $R = 0.15$. At 2 GHz, VSWR decreases toward unity when the opening size is increased from $W_t = 15\,\text{mm} \approx 0.1\lambda$, $W_t = 35\,\text{mm} \approx 0.23\lambda$, to $W_t = 60\,\text{mm} \approx 0.4\lambda$. The literature [10, 11] explained that the smaller aperture height profits the wider low end of frequency, which is in contrast to our result that smaller opening of tapered slot increases the VSWR. That difference happens because our antenna is designed with high opening rate R. For resonance at the low-end frequency, the antenna should be designed with tapered slot opening of wider mouth, while antennas with small R can be designed with small W_t. Figure 7 shows that at 3 GHz variation in W_t only slightly affects the resulting E-field, while at 5 GHz, a significant increase of E Field is observed for $W_t = 15\,\text{mm}$ (0.25λ), $W_t = 35\,\text{mm}$ (0.583λ) and $W_t = 60\,\text{mm}$ (1λ) in ascending order. At 7 GHz the same phenomenon happens for $W_t = 15\,\text{mm}$ (0.35λ), $W_t = 35\,\text{mm}$ (0.7λ) and $W_t = 60\,\text{mm}$ (1.4λ) in ascending order. Although the antenna exhibits S_{11} below $-10\,\text{dB}$ at 2–10 GHz, the performance of E-field is diverse for different values of W_t. For $R = 0.15$, and $W = 60\,\text{mm}$, enlarged tapered slot mouth opening yields an increase in E-fields.

2.4. Opening Rate of the Tapered Slot

The effect of opening rate R on VSWR, resistance, and reactance can be seen in Figure 8 by setting $L = 60\,\text{mm}$, $W = 60\,\text{mm}$, and $W_t = 30\,\text{mm}$. Figure 8(a) shows that smaller R yields worse VSWR for tapered slot length of $60\,\text{mm} \approx 0.6\lambda$ at 3 GHz, and $W_t = 30\,\text{mm}$. Decreasing VSWR value at low frequencies with the variation of R is obtained for $R = 0.01$, $R = 0.09$ and $R = 0.19$ respectively. At 2 GHz, increasing R, enlarges resistance as shown in the lower side of Figure 8(b). At 3 GHz, antenna with smaller R produces higher fluctuation of reactance than those with larger R as shown in the upper side of Figure 8(b).

The effect of modification of R on the performance of E-field at several frequencies is shown in

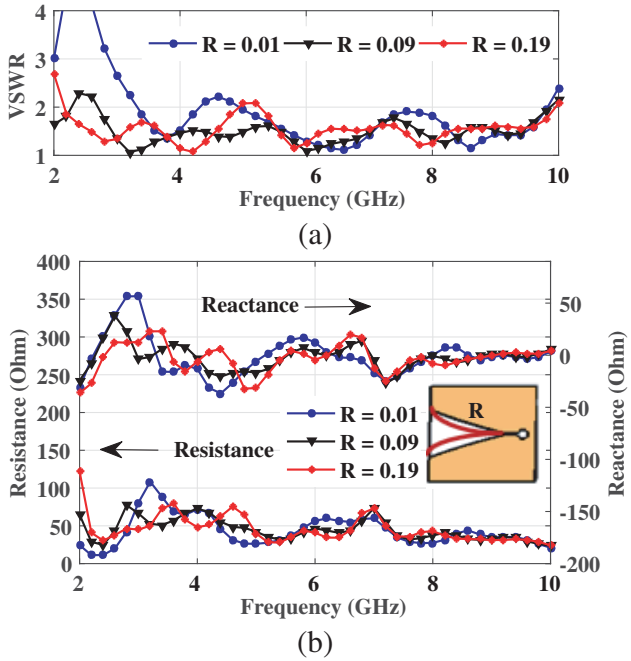

Figure 8. Effect of opening rate R of tapered slot (a) VSWR and (b) resistance and reactance with $L_t = 50\,\text{mm}$, $W = 60\,\text{mm}$ and $W_t = 30\,\text{mm}$.

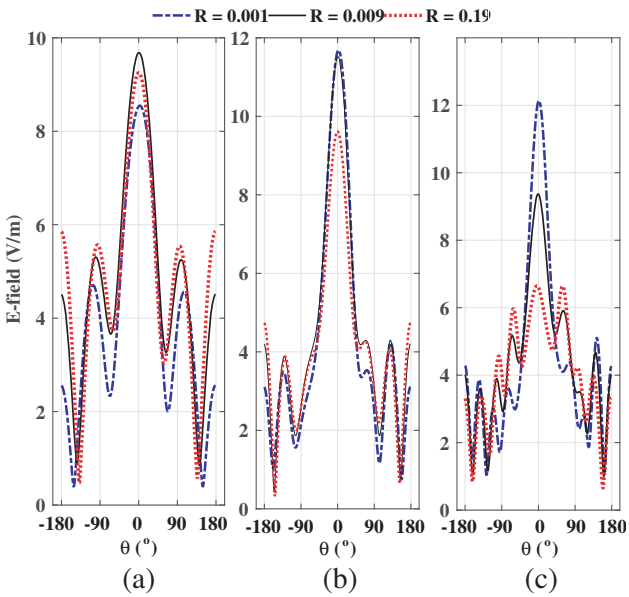

Figure 9. E-field on the E-plane with various opening rate R at frequency (a) 3 GHz, (b) 5 GHz and (c) 7 GHz with $L_t = 50\,\text{mm}$, $W = 60\,\text{mm}$ and $W_t = 30\,\text{mm}$.

Figure 9. At 3 GHz, the performances of E field are obtained for $R = 0.01$, $R = 0.19$ and $R = 0.09$, in ascending order. At 5 GHz, the antennas with $R = 0.09$ and $R = 0.01$ have similar E fields while the one with $R = 0.19$ results in the lowest E field. At 7 GHz the E-field performance is achieved for $R = 0.19$, $R = 0.09$ and $R = 0.001$, in the ascending order. At lower frequency, variation in the opening rate of the tapered slot yields different characteristics of the main lobe, side lobe and back lobe. At high frequency, increasing R yields decreasing E field performance.

2.5. Variation of Geometry to the *E*-Field Performance

Figure 10 depicts the effect of changes in geometry on the maximum E-field performance at frequency 3, 5 and 7 GHz. Figure 10(a) shows the maximum E-field performance with various element width by setting $L = 60$ mm, $W_t = 30$ mm and $R = 0.15$. It shows that the increase of element width yields escalation of E Field performance at 3 GHz. On the other hand, at 5 GHz, E-field increases and peaks at around $W = 55$ mm $\approx 0.92\lambda$ (5 GHz), and then declines. At 7 GHz, E Field tends to decrease with increasing antenna width because it has element width of more than 1λ.

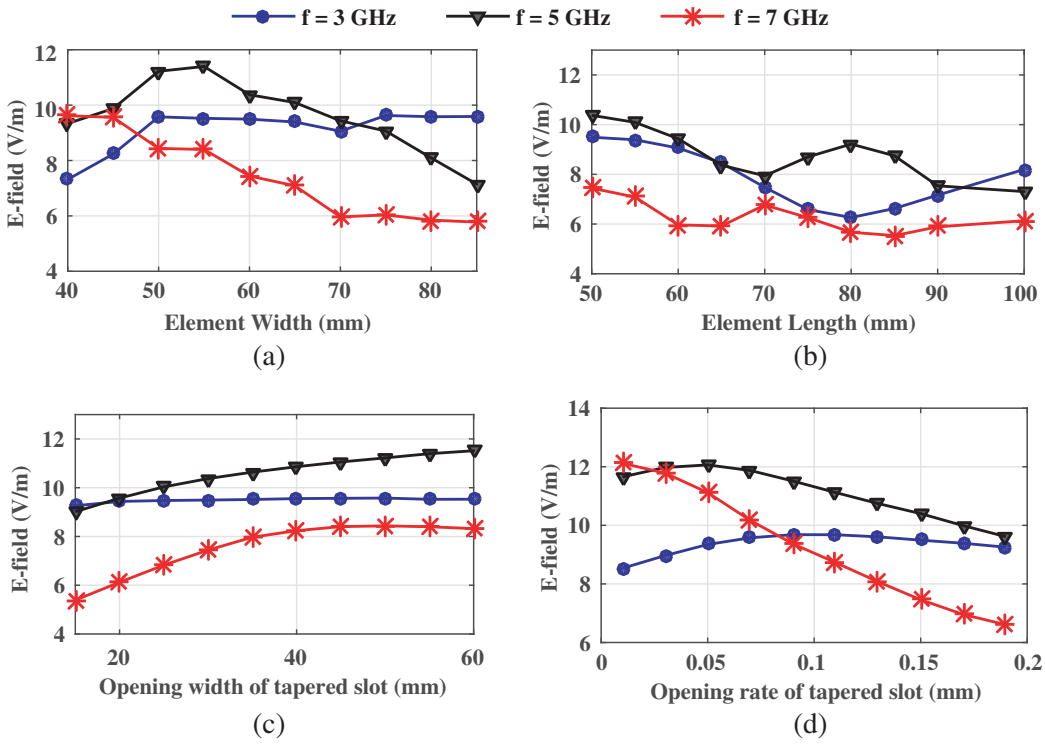

Figure 10. E-field performance on the E-plane with variation: (a) The width of element, (b) the length of tapered slot, (c) the opening width of tapered slot and (d) the opening rate.

Figure 10(b) reveals the impact of varying tapered slot length (L_t) to the E field at $W = 60$ mm, $W_t = 30$ mm and $R = 0.15$. It can be observed that the E field varies unequally at different frequencies. At 3 GHz, with $L_t > 50$ mm (0.5λ) the element experiences decreasing E field until $L_t = 80$ mm (0.8λ), after which it goes up. At 5 GHz, the E field decreases down to $L_t = 70$ mm (1.16λ), goes up again and peaks at $L_t = 80$ mm (1.33λ) then decreases again. At 7 GHz, variations of L_t with $W = 60$ mm, $W_t = 30$ mm and $R = 0.15$ result in the smallest E field in comparison to the other frequencies. It happens because at 7 GHz $L_t > 1\lambda$ for all values of L_t considered in this study. Lengthening the tapered slot results in the reduction of E field, especially at the high end of frequency band of interest if it is consistently more than 1λ at that particular frequency. At low frequencies the antenna resonates when it has a tapered length of some certain value around multiples of 0.5λ at its working frequency. Figure 10(c) explores variation of the tapered slot width to the E-field. It shows consistent E-field for

W_t varying from 15 mm to 60 mm at 3 GHz. At 5 GHz and 7 GHz, E-field increases with increasing width of the tapered slot by setting $L = 60$ mm, $W = 60$ mm and $R = 0.15$. The high value of R in small mouth opening W_t of the tapered slot causes the slope from the beginning of the slot to the middle to change only a little. Furthermore, the slope will change drastically at the opening end of the tapered slot. It affects the E-fields at high frequency. Figure 10(d) represents the effect of the slope of tapered slot to E-field performance by setting $L = 60$ mm, $W = 60$ mm and $W_t = 30$ mm. At 3 GHz, the greater R value, the greater the E field up to $R = 0.1$ after which the E-field comes down slowly. However, at 5 GHz and 7 GHz the greater R, the smaller E field. By setting W_t with fixed value, the greater R yields the smaller flare angle and throat in the beginning of the slot, and it governs E-field performance at high frequency.

3. ANTENNA PATTERN MODELLING

Results of study on Vivaldi antenna geometry and performance in Section 2 indicate that the radiation pattern depends on the antenna geometry parameters. In this section, we use the derivation of E-field of a horn antenna to find an approximation of the far field electric field modelling of Vivaldi antenna taking into account the geometry parameters. Figure 11(a) describes the spherical coordinate system with variables θ, ϕ and r which is used for reference to an observation point in the Cartesian coordinate system in Figure 11(b). These systems are used herein to explain the Vivaldi element modelling. Horn and Vivaldi antennas have the same feature of directional radiation pattern as shown in Figures 11(g) and (h), where the electric field propagates between tapered slots toward the mouth opening of tapered slot. The E field from a radiator can be derived by electric and magnetic potential vectors from electric and magnetic source current [27]. A wave can propagate in x, y and z direction with wave number k as:

$$k_x = k\cos\theta\sin\phi, \quad k_y = k\sin\theta\sin\phi, \quad k_y = k\cos\theta \tag{2}$$

Figure 11(b) describes the far field of an antenna, which can be observed with phase and magnitude:

$$R \cong r - r\cos\psi \text{ for phase variation}, \quad R \cong r \text{ for amplitude variation} \tag{3}$$

where R is the distance of charge density at any point to the observation point. The observation is considered to be in the far field if $R = 2D^2/\lambda$, with D denoting the largest dimension of antenna and

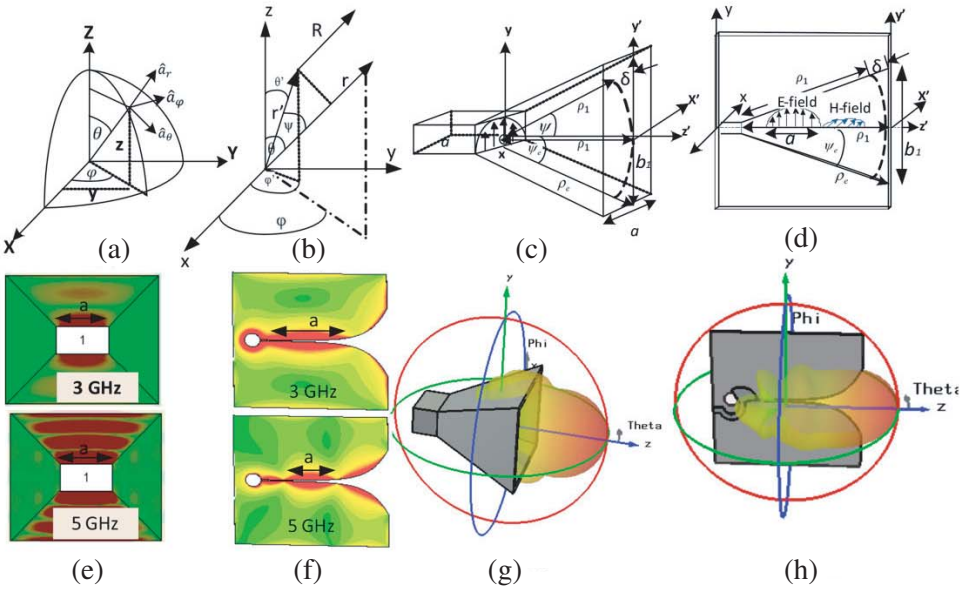

Figure 11. (a) Reference spherical coordinate, (b) reference rectangular coordinate, (c) horn antenna coordinate, (d) Vivaldi antenna coordinate, (e) 2D E-field of horn antenna, (f) 2D E-field of Vivaldi antenna, (g) 3D radiation pattern of horn antenna and (h) 3D radiation pattern of Vivaldi antenna.

λ the wavelength. In the far field, the radial distance R is parallel to the observation point r. It yields phase variation with ψ being the angle between r and r' see Figure 11(c)). The unprimed (x, y, z or r, θ, ϕ) indicate the observation point and the prime (x', y', z' or r', θ', ϕ') locates the electric and magnetic source in the space. In the far field the radial component is negligible, but component θ and ϕ is very dominant. To find the electric field, we extend the horn antenna feature to the Vivaldi having a tapered slot with linear slope. We suppose Vivaldi antenna in Figure 11(d) when designed with linear tapered slot has the same difference in path of travel as horn antenna in Figure 11(c). The difference in path is due to difference traveling wave referred by [27]:

$$\delta(y') = \frac{1}{2}\left(\frac{y'^2}{\rho_1}\right), \quad \rho_1 = \rho_e \cos\psi_e \tag{4}$$

Electromagnetic field in antenna is radiated by electric source $\mathbf{J}_s$ and magnetic source $\mathbf{M}_s$ that is propagated in all directions which combine with each other to form the electric and magnetic fields. To find the electric field, firstly we must find vector magnetic potential $\mathbf{A}$ and vector electric potential $\mathbf{F}$ due to electric density $\mathbf{J}$ and magnetic density $\mathbf{M}$ is given by surface integral:

$$\mathbf{A} \cong -\frac{\mu}{4\pi}\int\limits_S \mathbf{J}_s \frac{e^{-jkR}}{R} ds' \cong \frac{\mu e^{-jkr}}{4\pi r}\mathbf{N}, \quad \mathbf{N} \cong -\int\limits_S \mathbf{J}_s e^{-jkr'\cos\psi} ds' \tag{5}$$

$$\mathbf{F} \cong -\frac{\varepsilon}{4\pi}\int\limits_S \mathbf{M}_s \frac{e^{-jkR}}{R} ds' \cong \frac{\varepsilon e^{-jkr}}{4\pi r}\mathbf{L}, \quad \mathbf{L} \cong -\int\limits_S \mathbf{M}_s e^{-jkr'\cos\psi} ds' \tag{6}$$

$$E_\theta \cong -j\omega\left[A_\theta + \eta F_\varphi\right] = -\frac{jke^{-jkr}}{4\pi r}\left(L_\phi + \eta N_\theta\right) \tag{7}$$

where μ is the permeability, and ε is the permittivity or dielectric constant. We change the field representations from rectangular to spherical coordinate system:

$$N_\theta \cong -\int_S \left(J_x \cos\theta\cos\varphi + J_y \cos\theta \sin\varphi - J_z \sin\theta\right) e^{jkr'\cos\psi} ds \tag{8}$$

$$L_\varphi \cong \int_S \left(-M_x \sin\varphi + M_y \cos\varphi\right) e^{jkr'\cos\psi} ds' \tag{9}$$

For Vivaldi antenna, the electric and magnetic fields satisfy the following conditions: $E_x^{'} = E_z^{'} = H_y^{'} = 0$. In Vivaldi antenna, Electric field occupies the yz plane with maximum amplitude in y axis and propagates along the z axis as shown in Figure 11(d).

$$E_y^{'}\left(y', z'\right) \cong E_1 \cos\left(\frac{\pi}{a}z'\right) \exp\left(-j\frac{ky'^2}{(2\rho_1)}\right) \tag{10}$$

$$H_x^{'}\left(y', z'\right) \cong -\frac{E_1}{\eta}\cos\left(\frac{\pi}{a}z'\right) \exp\left(-j\frac{ky'^2}{(2\rho_1)}\right) \tag{11}$$

$$H_z^{'}\left(x', y'\right) \cong jE_1\left(\frac{\pi}{ka\eta}\right)\cos\left(\frac{\pi}{a}z'\right) \exp\left(-j\frac{ky'^2}{(2\rho_1)}\right) \tag{12}$$

E_1 is a constant, and those with a prime represent the fields in the aperture. Parameter a is a constant denoting the aperture dimension of horn antenna as shown in Figures 11(c) and (e), while in Vivaldi antenna the value of a varies with its operating frequency as in Figures 11(d) and 11(f). The E field of a horn antenna is in the xy plane, whereas that of a Vivaldi antenna is in the yz plane as shown in Figures 11(c) and (d). The electric and magnetic current densities can be expressed as:

$$J_y \cong -\frac{E_1}{\eta}\cos\left(\frac{\pi}{a}z'\right) e^{-j\left(ky'^2/(2\rho_1)\right)} - a/2 \le x' \le a/2 \tag{13}$$

$$M_x \cong E_1 \cos\left(\frac{\pi}{a}z'\right) e^{-j\left(ky'^2/(2\rho_1)\right)} - b_1/2 \le y' \le b_1/2 \tag{14}$$

$J_x = J_z = M_y = 0$. The electric field in a Vivaldi antenna propagates in the z axis with wavelength that depends on its operating frequency as shown in Figure 11(f). It governs the value of a in Equation (13), whereas the horn antenna has a constant value of a according to its geometry as shown in Figures 11(c) and (e). We take the value of $b1$ in Equation (14) to be the mouth opening of tapered slot which is similar to the horn antenna. To find E-field, firstly we find L_ϕ and N_θ by substituting the electric current density and magnetic current density from Equation (13) to Equation (8).

$$N_\theta = \int_s \left(-\frac{E_1}{\eta} \cos\left(\frac{\pi}{a} z'\right) e^{-jk(\delta(y'))} \cos\theta \sin\phi \right) e^{jk(y' \sin\theta \sin\phi + z' \cos\theta)} \tag{15}$$

the completion of the integral equation of the Equation (15) is as follows:

$$N_\theta = -\frac{E_1}{\eta} \cos\theta \sin\phi \left(\frac{-\pi a}{2}\right) \frac{\cos\left(\frac{ka}{2}\cos\theta\right)}{\left(\frac{ka}{2}\cos\theta\right)^2 - \left(\frac{\pi}{2}\right)^2} \sqrt{\frac{\pi\rho_1}{k}} e^{j\left(k_y^2 \rho_1 / 2k\right)} \left(F\left(t_1, t_2\right)\right) \tag{16}$$

where $F(t_1, t_2)$ is the Fresnel equation defined as:

$$F(t_1, t_2) = [C(t_2 - t_1)] - j(S(t_2) - (t_1))] \tag{17}$$

C is the real part, and S is the imaginary part of the Fresnel integral, while t_1 and t_2 are defined [27]:

$$t_1 = \sqrt{s}\left[-0.5 - 0.5\left(\frac{1}{s}\right)\left(\frac{b_1}{\lambda}\sin\theta\right)\right], \quad t_2 = \sqrt{s}\left[-0.5 - 0.5\left(\frac{1}{s}\right)\left(\frac{b_1}{\lambda}\sin\theta\right)\right] \tag{18}$$

where $s = \frac{1}{64}$. The solution to integral equation (18) is:

$$L_\phi = E_1 \sin\phi \int_{-a/2}^{a/2} \cos\left(\frac{\pi}{a} z'\right) e^{jkz' \cos\theta} dz \int_{-b/2}^{b/2} e^{-jk(\delta(y'))} e^{jk(y' \sin\theta \sin\phi)} dy \tag{19}$$

$$L_\phi = -E_1 \sin\phi \left(-\frac{\pi a}{2}\right) \frac{\cos\left(\frac{ka}{2}\cos\theta\right)}{\left(\frac{ka}{2}\cos\theta\right)^2 - \left(\frac{\pi}{2}\right)^2} \sqrt{\frac{\pi\rho_1}{k}} e^{j\left(\frac{k_y^2 \rho_1}{2k}\right)} F\left(t_1, t_2\right) \tag{20}$$

by substituting Equations (15) and (18) into Equation (6), we obtain:

$$E_\theta \cong -\frac{ja\sqrt{\pi k \rho_1} E_1 e^{-jkr}}{8r} \left(\cos\theta + 1\right) \sin\phi \frac{\cos\left(\frac{ka}{2}\cos\theta\right)}{\left(\frac{ka}{2}\cos\theta\right)^2 - \left(\frac{\pi}{2}\right)^2} e^{j\left(\frac{k_y^2 \rho_1}{2k}\right)} F\left(t_1, t_2\right) \tag{21}$$

From Equation (21), there is a part that greatly influences the shape of the main lobe and side lobe. If we separate the factors in Eq. (21) as given in Eqs. (22) and (23), different component patterns result as shown in Figure 12.

$$ML1 = -\frac{jE_1 a\sqrt{\pi k \rho_1} e^{-jkr}}{8r} \left(\cos\theta + 1\right), \quad ML2 = \sin\phi \frac{\cos\left(\frac{ka}{2}\cos\theta\right)}{\left(\frac{ka}{2}\cos\theta\right)^2 - \left(\frac{\pi}{2}\right)^2}, \quad ML3 = e^{j\left(\frac{k_y^2 \rho_1}{2k}\right)} \tag{22}$$

$$SL = F\left(t_1, t_2\right) \tag{23}$$

Figure 12 displays $ML1$, $ML2$, $ML3$ and SL patterns. As can be seen, multiplication of $ML1$, $ML2$, $ML3$ greatly contributes to the main lobe, while SL predisposes the side lobe level. The magnitude result of multiplication all parts of Equations (22) and (23) results in the pattern is shown in Figure 12(e). But if the multiplication result of $ML1$, $ML2$ and $ML3$, is added with SL, it will result the absolute

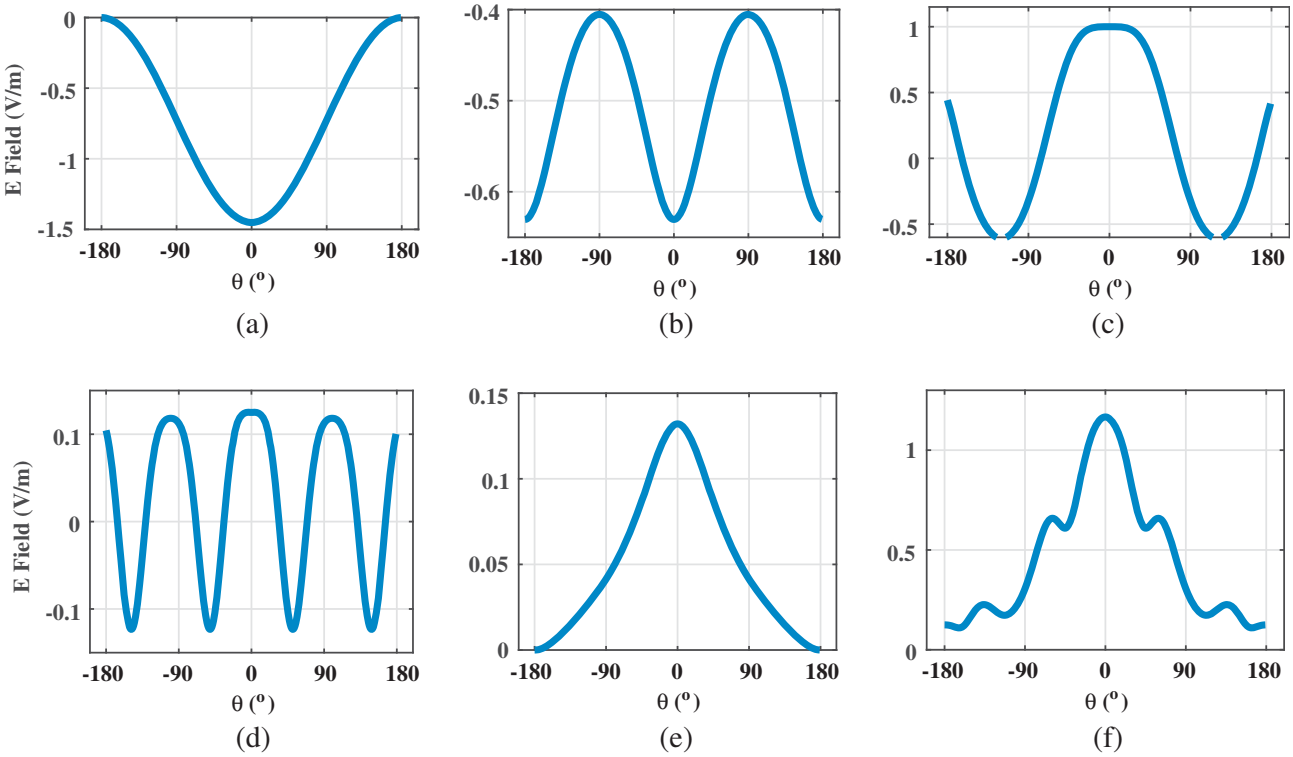

Figure 12. Components of Vivaldi element pattern model: Components of Vivaldi element pattern model: (a) $ML1$, (b) $ML2$, (c) $ML3$, (d) SL, (e) magnitude of multiplication of all components, (f) Magnitude of ML elements plus SL.

pattern in Figure 12(f). At 3 GHz, if we change the factor θ in k_y into $\frac{1}{2}\theta$, $ML3$ in Eq. (22) shows a better performance of E-field. The slope of the tapered slot is changed drastically at the end of the opening mouth of the tapered slot and it yields different phase at the low end of frequency. The resonance at 3 GHz can be shown in upper side of Figure 11(f). However, at 5 GHz, we have to replace theta in k_y with $\frac{3}{4}\theta$. The slope at the beginning and the middle of the tapered slot impacts the resonance at high-end frequencies expressed in lower side of Figure 11(f).

Based on the above results, we approximate the modelling E-field of Vivaldi Antenna as:

$$E_\theta \cong \left| \left(K_1 + K_2 \left(-\frac{jE_1 a\sqrt{\pi k\rho_1}e^{-jkr}}{8\,r}\left(\cos\theta+1\right)\frac{\cos\left(\frac{ka}{2}\cos\theta\right)}{\left(\frac{ka}{2}\cos\theta\right)^2-\left(\frac{\pi}{2}\right)^2}e^{j\left(\frac{k_y^2\rho_1}{2k}\right)}\right) + K_3\times F\left(t_1,t_2\right)\right)\right| \quad (24)$$

$$t_1 = \sqrt{s}\times\left(-K_4 - K_5\left(\frac{1}{s}\right)\times\left(\frac{b_1}{\lambda_0}\right)\times\sin\left(K_6\theta\right)\right) \quad (25)$$

$$t_2 = \sqrt{s}\times\left(K_4 - K_5\left(\frac{1}{s}\right)\times\left(\frac{b_1}{\lambda_0}\right)\times\sin\left(K_6\theta\right)\right) \quad (26)$$

where $r = 1\,\text{m}$, $E = 1\,\text{V/m}$, $\lambda_g = \frac{\lambda_0}{\sqrt{\varepsilon_r}} = \frac{\lambda_0}{\sqrt{\frac{1+\varepsilon_0}{2}}}$, $a = 0.5\lambda_g$, $b_1 = W_t$, $\rho_1 = L_t$, $K_1 = (2.5 - 0.1f)$, $K_2 = (f{+}0.3W{-}0.9)$, $K_3 = (2f{+}0.25W)$, $s = \frac{1}{64}$, $K_4 = (2{-}0.3f)$, $K_5 = (0.9{-}(0.01W^2{-}0.1W){-}0.13f)$, $K_6 = 0.9$.

Equation (24) is suitable for antenna with dimensions shown in Figure 1. Combination of constants in front of $ML1$, $ML2$, $ML3$, and SL greatly affects the shape of the E field. In the model evaluation in the next section, we examined E-field of Vivaldi antenna at 3 and 5 GHz only, with the width of element relative to its wavelength more than 0.5λ and less than 1λ.

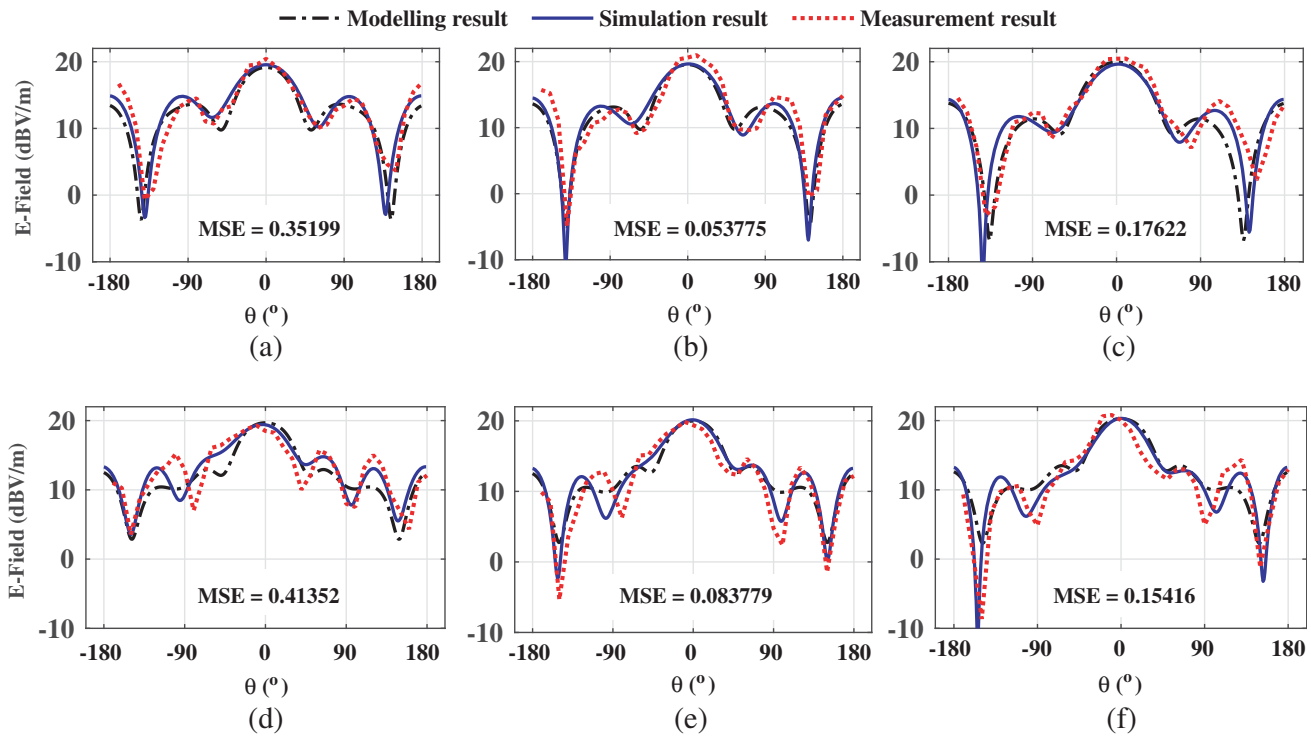

Figure 13. E field in decibel scale on the E-plane at: (a) $W = 6\,\text{cm}$, $f = 3\,\text{GHz}$, (b) $W = 7\,\text{cm}$, $f = 3\,\text{GHz}$, (c) $W = 8\,\text{cm}$, $f = 3\,\text{GHz}$ and (d) $W = 4\,\text{cm}$, $f = 5\,\text{GHz}$, (e) $W = 5\,\text{cm}$, $f = 5\,\text{GHz}$, (f) $W = 6\,\text{cm}$, $f = 5\,\text{GHz}$.

4. RESULT AND DISCUSSION

4.1. Vivaldi Antenna Element Modelling Result

Figure 13 shows comparison of modelling, simulation, and measurement results in decibel scale of (E_θ) as given in Eq. (24). Figures 13(a)–(c) show agreement between simulation and modelling for element widths 6 cm, 7 cm, and 8 cm at 3 GHz and so do Figures 13(d)–(f) for element widths 4 cm, 5 cm, and 6 cm at 5 GHz. There are more side lobes at 5 GHz than at 3 GHz. The wider the element is, the smaller the side lobe level is, as shown in Figures 13(a) and (c). The Fresnel equation in Eq. (24), which depends on t_1 and t_2, greatly influences the shape of the side lobe. By adjusting the constants K_4, K_5, and K_6 in Eqs. (25)–(26), the number and level of side lobes can be controlled, with t_1 and t_2. Figure 13 also demonstrates that increasing frequency will increase the level of the main lobe, which can be controlled by adjusting K_3 in Eq. (24). Figure 13(d) shows the asymmetry of side lobe from simulation, which is caused by the asymmetrical feeding structure, whereas the approximation model shows a symmetrical pattern because it is modeled with $t_1 = t_2$. When it is required to model asymmetrical side lobe, t_1 and t_2 should be designed with non identical constants.

We use the value of Mean Square Error (MSE) to measure the accuracy of a model with our simulation results. The smallest MSE is obtained for antenna element with $W = 7\,\text{cm}$, and $f = 3\,\text{GHz}$ is 0.053775, while the largest MSE is obtained for $W = 4\,\text{cm}$, and $f = 5\,\text{GHz}$ is 0.41352. Figure 14 presents the results of the S_{11} measurement using a Vector Network Analyzer and radiation pattern measurement with a spectrum analyzer.

Table 2 tabulates the performance of the antenna in gain, beam width, first side lobe level, and back lobe observed from Figure 13. The table indicates that increasing the width of element decreases the peak of side lobe level. It can be shown that for element width of 6 cm, the modelling result yields SLL of $-5.53\,\text{dB}$, but for element width of 8 cm the modelling yields SLL of $-6.1\,\text{dB}$. Table 2 shows that there are slight differences in beamwidth, first SLL, and back lobe among all elements, but agreement between modelling and simulation results is maintained.

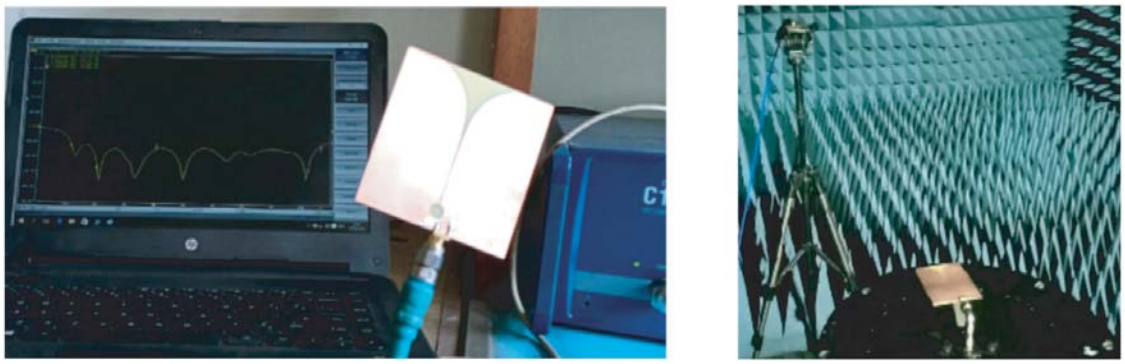

(a) (b)

Figure 14. (a) S_{11} measurement and (b) radiation pattern measurement.

Table 2. Comparison of modelling and simulation result.

frequency	$f = 3\,\text{GHz}$					
Parsmeter	$W = 6\,\text{cm} = 0.6\lambda$		$W = 7\,\text{cm} = 0.7\lambda$		$W = 8\,\text{cm} = 0.8\lambda$	
Result in	Modelling	Simulation	Modelling	Simulation	Modelling	Simulation
MainLobe (dBV/m)	19.15	19.5	19.55	19.8	19.94	19.9
3 dB BW (Deg)	62	65.4	62	63.5	62	61.1
1st SLL (dB)	−5.53	−4.2	−5.93	−4.8	−6.1	−5.1
Backlobe (dB)	13.44	15.23	13.49	14.97	13.78	14.82
frequency	5 GHz					
Parsmeter	$4\,\text{cm} = 0.67\lambda$		$5\,\text{cm} = 0.83\lambda$		$6\,\text{cm} = 1\lambda$	
Result in	Modelling	Simulation	Modelling	Simulation	Modelling	Simulation
Main Lobe (dBV/m)	19.68	19.3	19.98	20.1	20.27	20.5
3 dB BW (Deg)	68	68.6	58	58	60	53.3
1st SLL (dB)	−6.75	−4.3	−6.44	−5.6	−6.82	−6.1
Baclobe (dB)	12.5	14.9	12.53	14.5	12.62	14.31

4.2. Variation Variable of Vivaldi Antenna Modelling

Coefficients a, ρ_1, $K_{1\text{-}6}$ in Eqs. (24), (25), and (26) can influence the E field performance. Figure 15 shows the differences in performance of E-field when a is varied for an antenna with fixed dimensions, in this case $L = 6\,\text{cm}$, $W = 6\,\text{cm}$ at the frequency of 3 GHz. Coefficient a influences the elevation of main lobe, SLL, and beamwidth. In general, the larger the value of a is, the higher the main lobe is, and the smaller the beamwidth is. The main lobe for $a = 0.8\lambda_g$, which is the largest examined herein for 3 GHz frequency, is larger than those for others. It is also shown that while the beam width is the smallest, there are no changes in back lobe level. In addition, the higher the value of a is, the shallower the null of the first side lobe level is as shown in Figure 15. Coefficient ρ_1 is related with phase variation in each frequency and responsible for the main lobe and side lobe performance. The greater the value of ρ_1 is, the higher the level of main lobe is, and the greater the number of side lobes is as shown in Figure 16. Comparison between $\rho_1 = 0.25$ and $\rho_1 = 14.25$ shows that higher values of ρ_1 yield more side lobes. Changes in value of coefficient K_1 in Eq. (24) shift the overall curve upwards as shown in Figure 17. Higher values of K_1 lead to higher levels of the main lobe, side lobe level, back lobe, and first null. The higher the value of K_2 is in Eq. (24), the significantly higher the level of main lobe, side lobe, and first null are, but there is no change in the back lobe level and beamwidth, as shown in Figure 18.

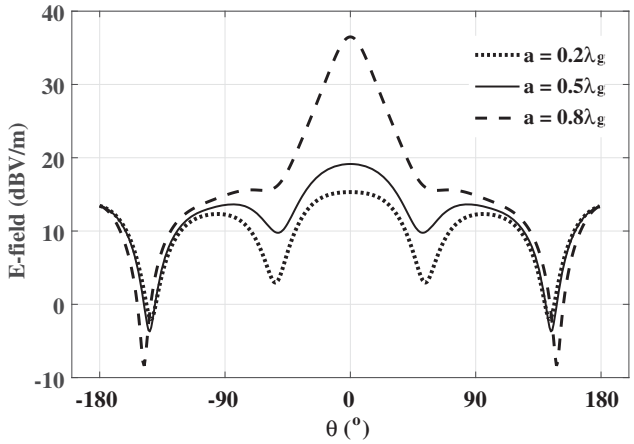

Figure 15. Modelling result of E-field on the E-plane with variation of parameter a.

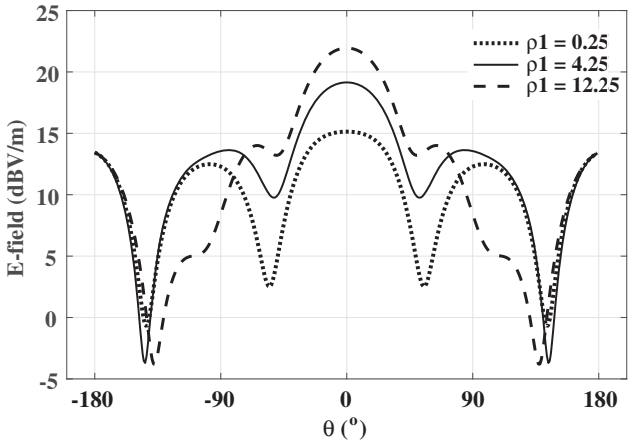

Figure 16. Modelling result of E-field on the E-plane with variation of parameter ρ.

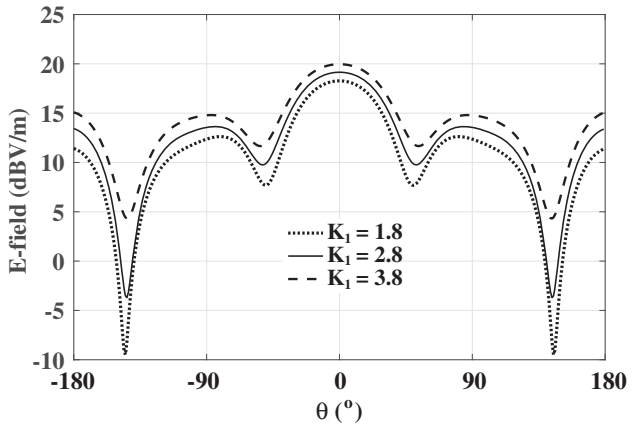

Figure 17. Modelling result of E-field on the E-plane with variation of parameter K_1.

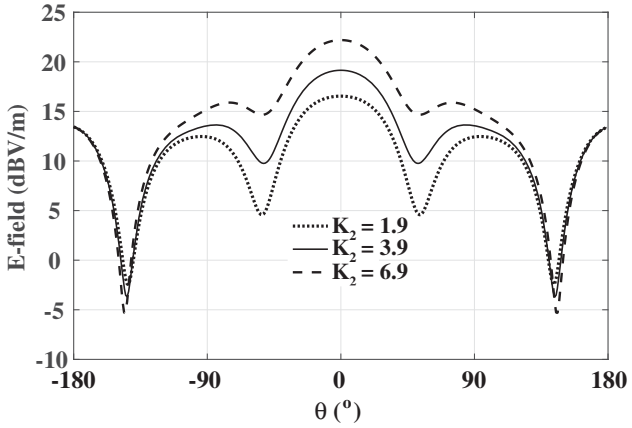

Figure 18. Modelling result of E-field on the E-plane with variation of parameter K_2.

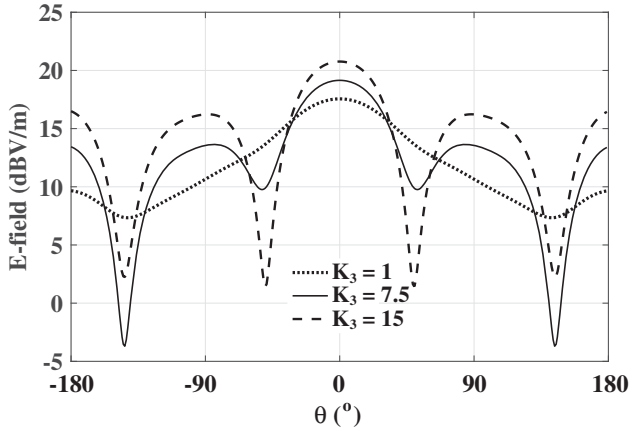

Figure 19. Modelling result of E-field on the E-plane with variation of parameter K_3.

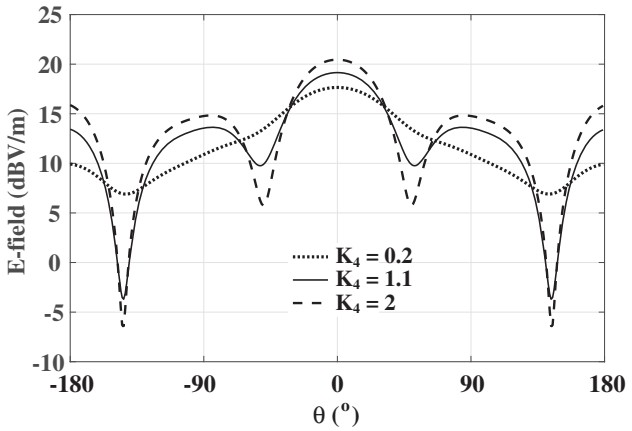

Figure 20. Modelling result of E-field on the E-plane with variation of parameter K_4.

Figure 19 and Figure 20 present the impact of changes in the values of K_3 and K_4 on Equations (24) and (25), respectively. Incremental values of K_3 and K_4 can increase main lobe, side lobe, and back lobe. The higher values of K_3 and K_4 result in the shallower null of the first and second side lobe levels of E-field performance. Variation in the Fresnel function is shown in Figures 20–22. Parameter t_1 greatly influences the side lobe on the right side, so does t_2 on the left side. The number of side lobes can be changed by varying the constant K_5. Enlarging the value of K_5 will reduce beamwidth and increase the number of side lobes, but maintain the level of main lobe and back lobe. Increasing the number of side lobes can be done by enhancing the value of K_5 in the bracketted part of t_1 and t_2 in Eqs. (25) and (26), respectively. Figure 22 shows the different phases of side lobe and different nulls of side lobe by maintaining the level of main lobe. Reducing the value of K_6 can extend the beamwidth of the side lobe. Based on Eqs. (24)–(26) and the results in Figures 15–22, another model of Vivaldi antenna element can be developed according to its feeding shape, radiator shape, and operating frequency.

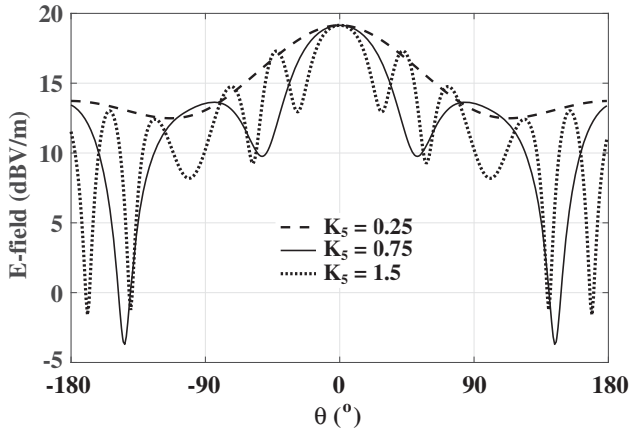

Figure 21. Modelling result of E-field on the E-plane with variation of parameter K_5.

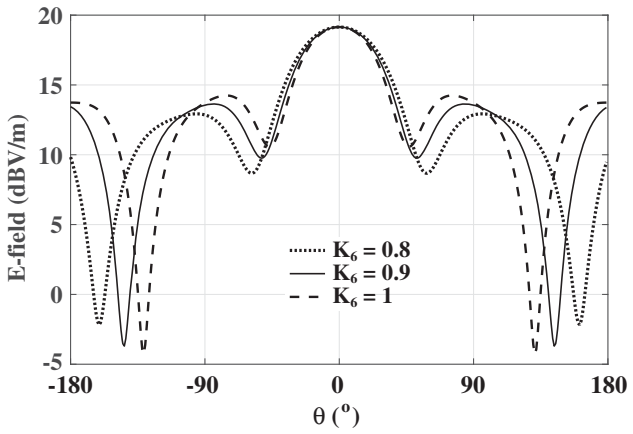

Figure 22. Modelling result of E-field on the E-plane with variation of parameter K_6.

5. APPLICATION TO ARRAY PATTERN MULTIPLICATION

The total array pattern of a Uniform Linear Array (ULA) can be obtained by multiplication of the element pattern and array factor. Figures 23–24 compare the total array patterns between modelling and simulation result. The modelling result is obtained from multiplication of the Vivaldi element model found from Equations (24)–(26) and the factor array.

$$AP_{tot} = E_\theta \times AF \tag{27}$$

where AP_{tot} is total array pattern, E_θ the element pattern, and AF the array factor of the antenna

$$AF = \sum_{n=1}^{N} w_n e^{j\psi_n} \tag{28}$$

$$w_n = a_n e^{j\delta_n} \tag{29}$$

$$\psi_n = kd_n \sin\theta + \beta \tag{30}$$

$$k = 2\pi/\lambda \tag{31}$$

$$\beta_n = -kd_n \sin\theta_0 \tag{32}$$

where w_n is the complex weight for element, N the number of elements, ψ the progressive phase of the n-th element, d the element separation, and β_n the phase excitation difference.

We simulate antenna array with four elements with 1 cm spacing between elements. Figures 23 and 24 are obtained for such an array with antenna element width of 6 cm at 3 GHz and 5 GHz, successively. From the figure we observe that between -50 and 50 degrees there is significant agreement

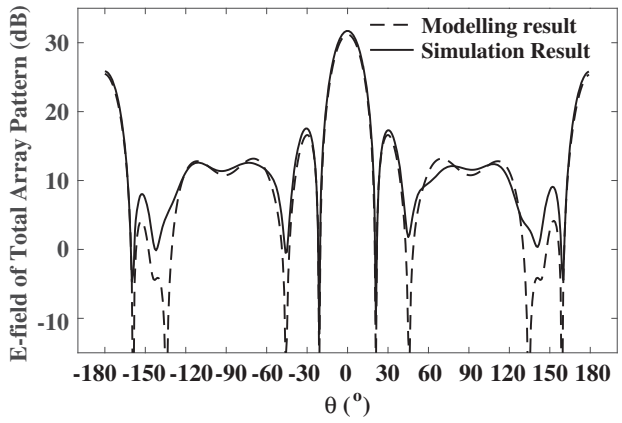

Figure 23. Total array pattern on the E-plane at 3 GHz, $N = 4$, $W = 6$ cm.

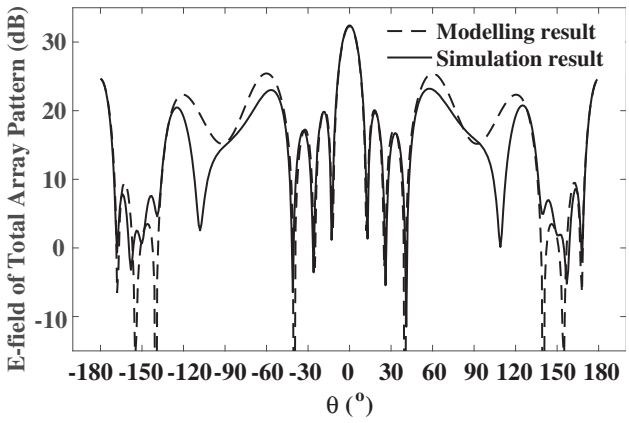

Figure 24. Total array pattern on the E-plane at 5 GHz, $N = 4$, $W = 6$ cm.

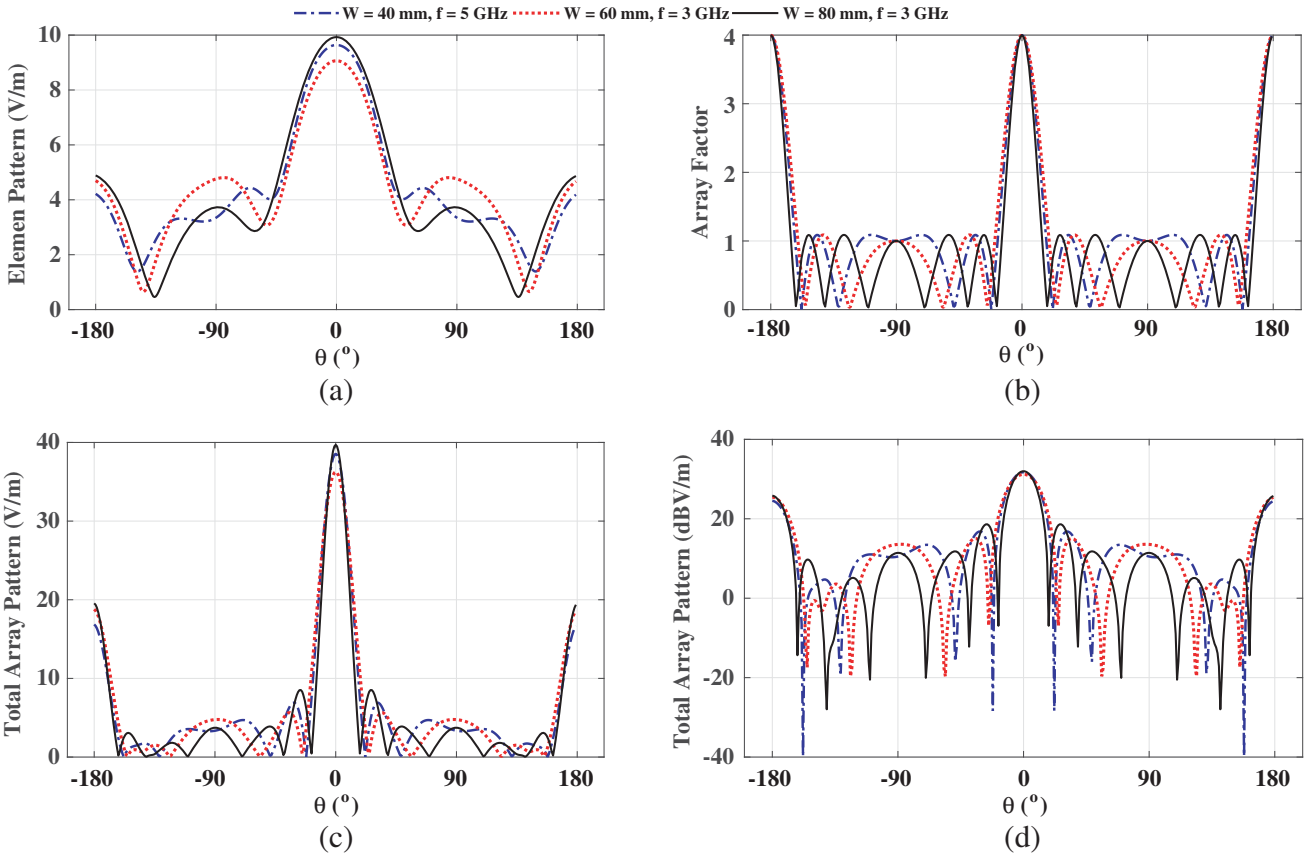

Figure 25. E-field pattern on the E-plane for different widths: (a) Element pattern, (b) array factor with $d = W$, (c) total array pattern (linear scale), (d) total array pattern (dB scale), with $N = 4$ and no spacing between element.

between total arrays patterns from modelling and simulation. There is only a slight difference in side lobe levels and nulls. From the figure we can see that the results for main lobe, first side lobe, and first null are in general agreement between simulation and model, which sufficiently justifies the usefulness of modelling approach for array pattern analysis. Furthermore, the total array pattern from the model can be developed for higher number of elements, even up to a thousand elements, with significantly reduced computation time compared to simulation based on numerical electromagnetic computation.

Figures 25(a) and (b) shows the impact of different element widths to the total linear array pattern. In the same frequency, increasing element width can enlarge mainlobe of total array pattern which can be observed in Figure 25(c) for element width of 6 cm and 8 cm. Antennas with element width of 4 cm at 5 GHz have higher main lobe of total array pattern than element width 6 cm at 3 GHz for the same number of elements. It results from antenna with element width 4 cm has higher gain than antenna with element width 6 cm.

Overall, using the approximation model of the Vivaldi element pattern, one can flexibly achieve array pattern analysis involving arbitrary number of elements and various forms of array, while at the same time saving the computation time. The only difference from the numerical result of electromagnetic computation approach is the absence of mutual coupling impact, which means that the modelling approach approximates the simulation result when mutual coupling between elements is negligible, i.e., when element spacing is sufficiently large.

6. CONCLUSIONS

We have analyzed the impact of variation in various parameters of a Vivaldi antenna, including the element width, the length of tapered slot, the mouth opening of tapered slot, and the opening rate of tapered slot, on such performance indicators as VSWR, resistance, reactance, and radiation pattern. VSWR, impedance, and E-field performances for various geometries can be used as a reference to design a Vivaldi antenna element. Although Vivaldi antenna can be designed with VSWR less than 2 in ultra-wideband frequency, it yields a different performance of radiation pattern in each operating frequency. Following the analysis, we have also found an approximation model of electric field of a Vivaldi antenna element having element width of more than 0.5λ and less than 1λ at 3 GHz and 5 GHz. The modelling result can be used further to analyze the pattern of a total array with varying number of elements and various array forms by pattern multiplication. This method reduces the computation time and increases flexibility in design and evaluation of Vivaldi antenna array with a large number of elements as long as the effect of mutual coupling is negligible.

ACKNOWLEDGMENT

This work has been supported by the BPPDN (Beasiswa Pendidikan Pascasarjana Dalam Negeri) funding program.

REFERENCES

1. Gibson, P. J., "The Vivaldi aerial," *Proc. 9th European Microwave Conf.*, 101–105, 1979.
2. Natarajan, R., J. V. George, M. Kanagasabai, L. Lawrance, B. Moorthy, D. B. Rajendran, and M. Alsath, "Modified antipodal Vivaldi antenna for ultrawideband communication," *IET Microwaves, Antennas & Propagation*, Vol. 10, No. 4, 401–405, 2016.
3. Ma, K., Z. Zhao, J. Wu, S. M. Ellis, and Z.-P. Nie, "A printed Vivaldi antenna with improved radiation patterns using two pairs of eye-shaped slots for UWB applications," *Progress In Electromagnetics Research*, Vol. 148, 63–71, 2014.
4. Wang, P., H. Zhang, G. Wen, and Y. Sun, "Design of modified 6–18 GHz balanced antipodal Vivaldi antenna," *Progress In Electromagnetics Research C*, Vol. 25, 271–285, 2012.
5. Fioranelli, A., S. Salous, I. Ndip, and X. Raimundo, "Through-the-wall detection with gated FMCW signals using optimized patch-like and Vivaldi antennas," *IEEE Trans. Antennas Propag.*, Vol. 63, No. 3, 1106–1116, 2015.
6. Yang, Y., Y. Wang, and A. E. Fathy, "Design of compact Vivaldi antenna arrays for UWB see through wall applications," *Progress In Electromagnetics Research*, Vol. 82, 401–418, 2008.
7. Yan, J. B., S. Gogineni, B. C. Raga, and J. Brozena, "A dual-polarized 2–18 GHz Vivaldi array for airbone radar measurement of snow," *IEEE Trans. Antennas Propag.*, Vol. 64, No. 2, 781–785, Feb. 2016.

8. Natarajan, R., M. Kanagasabai, and J. V. George, "Design of X-band Vivaldi antenna with low radar cross section," *IET Microwaves, Antennas & Propagation*, Vol. 10, No. 6, 651–655, 2016.
9. He, S. H., W. Shan, C. Fan, Z. C. Mo, F. H. Yang, and J. H. Chen, "An improved Vivaldi antenna for vehicular wireless communication systems," *IEEE Antennas Wireless Propag. Lett.*, Vol. 13, 1505–1508, 2014.
10. Moosazadeh, M., S. Kharkovsky, J. T. Case, and B. Samali, "UWB antipodal Vivaldi antenna for microwave imaging of construction materials and structures," *Microwave and Optical Technology Letters*, Vol. 59, No. 6, 1259–1264, 2017.
11. Esmati, Z. and M. Moosazadeh, "Reflection and transmission of microwaves in reinforced concrete specimens irradiated by modified antipodal Vivaldi antenna," *Microwave and Optical Technology Letters*, Vol. 60, No. 9, 2113–2121, 2018.
12. Moosazadeh, M., "High-gain antipodal Vivaldi antenna surrounded by dielectric for wideband applications," *IEEE Trans. Antennas Propag.*, Vol. 66, No. 8, 4349–4352, 2018.
13. Nurhayati, G. Hendrantoro, T. Fukusako, and E. Setijadi, "Mutual coupling reduction for a UWB coplanar Vivaldi array by truncated and corrugated," *IEEE Antennas Wireless Propag. Lett.*, Vol. 17, No. 12, 2284–2288, Dec. 2018.
14. Shin, J. and D. H. Schaubert, "A parameter study of stripline-fed Vivaldi notch-antenna arrays," *IEEE Trans. Antennas Propag.*, Vol. 47, No. 5, 879–886, May 1999.
15. Chio, T. H. and D. H. Schaubert, "Parameter study and design of wide-band widescan dual-polarized tapered slot antenna arrays," *IEEE Trans. Antennas Propag.*, Vol. 48, No. 6, 879–886, 2000.
16. Nurhayati, G. Hendrantoro, and E. Setijadi, "Effect of Vivaldi element pattern on the uniform linear array pattern," *IEEE International Conference on Communication, Networks and Satellite*, 42–47, 2016.
17. Nurhayati, G. Hendrantoro, and E. Setijadi, "Total array pattern characteristics of coplanar Vivaldi antenna in E-plane with different element width for S and C band application," *Progress In Electromagnetics Research Symposium Abstracts*, 604–612, Singapore, Nov. 19–22, 2017.
18. Schaubert, D. H., "Wide-band phased arrays of Vivaldi notch antennas," *International Conference on Antennas and Propagation*, 6–12, Apr. 1997.
19. Mailloux, R. J., *Phased Array Antenna Handbook*, Artech House, Boston, London, 2005.
20. Reid, E. W., L. O. Balbuena, A. Ghadiri, and K. Moez, "A 324-element Vivaldi antenna array for radio astronomy instrumentation," *IEEE Trans. Antennas Propag.*, Vol. 61, No. 1, 241–249, Jan. 2016.
21. Kindt, R. W. and W. R. Pickles, "Ultrawideband all-metal flared-notch array radiator," *IEEE Trans. Antennas Propag.*, Vol. 58, 3568–3575, Nov. 2010.
22. Vescovo, R., "Constrained and unconstrained synthesis of array factor for circular arrays," *IEEE Trans. Antennas Propag.*, Vol. 43, 1405–1410, Dec. 1995.
23. Florence, P. V. and G. S. N. Raju, "Optimization of linear dipole antenna array for sidelobe reduction and improved directivity using APSO algorithm," *IOSR Journal of Electronics and Communication Engineering*, Vol. 9, 17–27, 2014.
24. Mohammadian, H., N. M. Martin, and D. W. Griffin, "A theoretical and experimental stufy of mutual coupling in microstrip antenna arrays," *IEEE Trans. Antennas Propag.*, Vol. 37, 1217–1223, Oct. 1989.
25. Janaswamy, R. and D. H. Schaubert, "Analysis of the tapered slot antenna," *IEEE Trans. Antennas Propag.*, Vol. 39, No. 9, 1058–1065, Sep. 1987.
26. Janaswamy, R. and D. H. Schaubert, "Characteristic impedance of wide slotline on low-permitivity substrate," *IEEE Trans. on Microwave Theory and Techniques*, Vol. 34, 900–902, Sep. 1986.
27. Balanis, A. C., *Antenna Theory Analysis and Design*, John Wiley & Sons, Arizone State University, 1997.